ISSN 1541-308X, Physics of Wave Phenomena, 2007, Vol. 15, No. 2, pp. 81–94. © Allerton Press, Inc., 2007.

INTERACTION OF LASER RADIATION WITH MATTER

Photoacoustic Effect upon Material Melting and Evaporation by Laser Pulses

V. I. Mazhukin[a], N. M. Nikiforova[b], and A. A. Samokhin[c]

[a] *Institute for Mathematical Modeling, Russian Academy of Sciences, Moscow, 125047 Russia*
[b] *Moscow Lomonosov State University, Moscow, 119992 Russia*
Prokhorov General Physics Institute, Russian Academy of Sciences, Moscow, 119991 Russia
E-mail: asam40@mail.ru

Received November 17, 2006

Abstract — Photoacoustic signals in laser-irradiated samples were mathematically modeled for the cases when melting and evaporation occur. In particular, it was shown that rapid melting processes induced by nanosecond laser pulses result in a rather narrow pressure peak or dip in photoacoustic pressure signals due to density changes in the moving melting front. Amplitudes of these peaks or dips depend on the melting front velocity, as well as on the magnitude of density change. Experimental detection of this effect using a piezoelectric transducer requires a uniform laser intensity distribution over the irradiation spot.

PACS numbers: 43.35.Ud, 78.20.Hp, 79.20.Ds
DOI: 10.3103/S1541308X07020021

1. INTRODUCTION

The effect of pulsed laser radiation on absorbing condensed media is accompanied by generation of sound or shock waves carrying information on processes in the irradiated region (see, for example, [1–3] and references therein). The occurring photoacoustic effect can be caused by various physical mechanisms responsible for a change in a specific material volume upon radiation absorption, i.e., ordinary (equilibrium) heating, non-equilibrium (non-thermal) excitation of the electronic subsystem, or the first-order phase transitions.

Pressure pulses excited in a medium can be measured, for example, from an irradiated sample back side using proper piezoelectric transducers with a resolution of ~ 1 ns. The potential of photoacoustic diagnostics for studying the non-equilibrium first-order phase transitions such as melting or evaporation is still far from fully realized. In particular, this is because of the absence of sufficiently detailed theoretical studies of the dynamics of rapid phase transitions under laser exposure conditions, which can be performed only using modern methods of mathematical modeling.

In this paper, we consider the photoacoustic effect features associated with material melting and evaporation in the laser irradiation region. The statement of the problem and its numerical solution are described in Secs. 2 and 3, respectively. Section 4 is devoted to the analysis of the data obtained.

2. PROBLEM STATEMENT

A laser pulse with intensity $G = 10^7$–10^{10} W·cm^{-2} is absorbed in a narrow surface region of a target whose heating can be accompanied by phase transitions. The irradiation spot size is assumed to be much larger than the laser radiation absorption depth which is inversely proportional to the absorbance and the thermal heating depth during the laser pulse. This allows one to use a one-dimensional space approximation for mathematical description (Fig. 1).

In the general case, theoretical description of the dynamics of the first-order phase transition is a very complex problem and reduced to one the versions of the Stefan problem [4]. The classical version of the Stefan problem, formulated for melting–crystallization phase transitions, is reduced to the nonlinear heat conduction equation in a region with an a priori unknown interface Γ_{sl} between solid and liquid phases with temperature T_{sl} equal to the melting point T_m. Surface evaporation with the Mach number $M = 1$ in a evaporated material flow is described using the single-

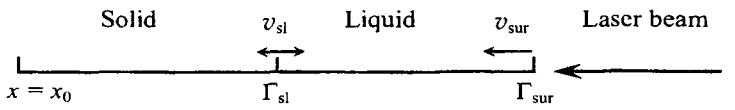

Fig. 1. Schematic representation of laser exposure and phase front propagation.

phase version of the Stefan problem [5], in which the evaporated surface temperature T_{sur} weakly (logarithmically) depends on the front Γ_{lv} velocity v_{lv} over the condensed phase.

The formation and propagation of the photoacoustic signal are mathematically modeled within the combined version of the Stefan hydrodynamic problem [6], including both (classical and single-phase) versions. The combined version is based on the complete set of hydrodynamic equations, complemented by the transport equation of laser radiation. The complete set of hydrodynamic equations consists of the continuity, motion, and total energy equations, considering convective, conductive, and radiative transport mechanisms. In the strictly divergent form, the set of equations is written as

$$\left[\frac{\partial \rho}{\partial t} + \frac{\partial}{\partial x}(\rho u) = 0\right]_k, \quad (1)$$

$$\left[\frac{\partial}{\partial t}(\rho u) + \frac{\partial}{\partial x}\left(\rho u^2\right) = -\frac{\partial p}{\partial x}\right]_k, \quad (2)$$

2.1. Formulation of Boundary Conditions

Boundary conditions. The left boundary $x = x_0$ was assumed to be fixed and heat-insulated,

$$\lambda \frac{\partial T}{\partial x} = 0, \quad u = 0. \quad (5)$$

At the melting front $x = \Gamma_{sl}(t)$, three conservation laws are written, complemented by the continuity condition of phase transition temperature:

(i) the mass conservation law

$$\rho_s v_{sl} = \rho_l \left(u_s - u_l + v_{sl}\right); \quad (6)$$

(ii) the momentum conservation law

$$\rho_s v_{sl}^2 + p_s = \rho_l \left(u_s - u_l + v_{sl}\right)^2 + p_l; \quad (7)$$

(iii) the energy conservation law (the differential Stefan condition)

$$\lambda_l \frac{\partial T_l}{\partial} - \lambda_s \frac{\partial T_s}{\partial} = L_m^{ne} \rho_s v_{sl}, \quad (8)$$

82 MAZHUKIN et al.

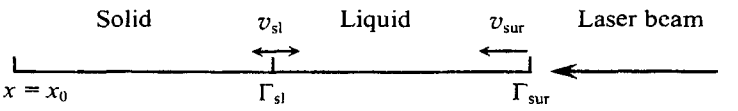

Fig. 1. Schematic representation of laser exposure and phase front propagation.

phase version of the Stefan problem [5], in which the evaporated surface temperature T_{sur} weakly (logarithmically) depends on the front Γ_{lv} velocity v_{lv} over the condensed phase.

The formation and propagation of the photoacoustic signal are mathematically modeled within the combined version of the Stefan hydrodynamic problem [6], including both (classical and single-phase) versions. The combined version is based on the complete set of hydrodynamic equations, complemented by the transport equation of laser radiation. The complete set of hydrodynamic equations consists of the continuity, motion, and total energy equations, considering convective, conductive, and radiative transport mechanisms. In the strictly divergent form, the set of equations is written as

$$\left[\frac{\partial \rho}{\partial t} + \frac{\partial}{\partial x}(\rho u) = 0\right]_k, \quad (1)$$

$$\left[\frac{\partial}{\partial t}(\rho u) + \frac{\partial}{\partial x}\left(\rho u^2\right) = -\frac{\partial p}{\partial x}\right]_k, \quad (2)$$

2.1. Formulation of Boundary Conditions

Boundary conditions. The left boundary $x = x_0$ was assumed to be fixed and heat-insulated,

$$\lambda \frac{\partial T}{\partial x} = 0, \quad u = 0. \quad (5)$$

At the melting front $x = \Gamma_{sl}(t)$, three conservation laws are written, complemented by the continuity condition of phase transition temperature:

(i) the mass conservation law

$$\rho_s v_{sl} = \rho_l \left(u_s - u_l + v_{sl}\right); \quad (6)$$

(ii) the momentum conservation law

$$\rho_s v_{sl}^2 + p_s = \rho_l \left(u_s - u_l + v_{sl}\right)^2 + p_l; \quad (7)$$

(iii) the energy conservation law (the differential Stefan condition)

$$\lambda_l \frac{\partial T_l}{\partial} - \lambda_s \frac{\partial T_s}{\partial} = L_m^{ne} \rho_s v_{sl}, \quad (8)$$

$$W_1^T = \lambda_1 \frac{\partial T_1}{\partial x} = \rho_1 v_{1v} L_v^{ne}, \tag{12}$$

$$L_v^{ne} = L_v(T_1) + c_{pv}(T_1 - T_v) + \frac{\rho_1 + \rho_v}{\rho_1 - \rho_v} \frac{(u_1 - u_v)^2}{2},$$
$$G_{1v} = A(T_{sur})\, G_0 \exp\left[-4\left(\frac{t}{t_0}\right)^2\right]. \tag{13}$$

The values of T_v, ρ_v, and p_v are determined from the relations on the non-equilibrium Knudsen layer using the Crout model [7, 8],

$$T_v = T_1 \alpha_T(M),$$
$$\rho_v = \rho_{sat} \alpha_\rho(M), \tag{14}$$
$$p_v = R \rho_v T_1,$$

where $M = u_v/c_s$ is the Mach number, $c_s = \sqrt{\gamma R T_v}$ is the speed of sound on the outer side of the Knudsen layer, $\alpha_T(M)$ and $\alpha_\rho(M)$ are the kinetic coefficients taking on the values of $\alpha_T(M) = 0.633$ and $\alpha_\rho(M) = 0.326$ at $M = 1$.

The saturated vapor pressure was calculated from the Clapeyron–Clausius equation,

$$p_{sat} = R \rho_{sat} T_1,$$
$$p_{sat} = p_b \exp\left[\frac{L_v}{R T_b}\left(1 - \frac{T_b}{T_1}\right)\right], \tag{15}$$

where p_b and T_b are the pressure and equilibrium boiling point under normal conditions, respectively.

Initial conditions. $t = t_0$: $T_s = T_0$, $u_s = 0$, $\rho_s = \rho_{0,s}$.

2.2. Optical and Thermal Characteristics of a Target

The melting surface absorptivity A_{sur} and the radiation density released in this case were determined by solving the problems of the two-layer system reflectivity (see [9]),

$$A_{sur} = 1 - R_{sur}, \tag{16}$$

where

$$R_{sur} = \left(\delta_1 + \frac{ar\exp(-\alpha_1 \Delta x_1)}{r^2 + \gamma^2}\right)^2 + \left(\frac{a\gamma \exp(-\alpha_1 \Delta x_1)}{r^2 + \gamma^2}\right)^2,$$

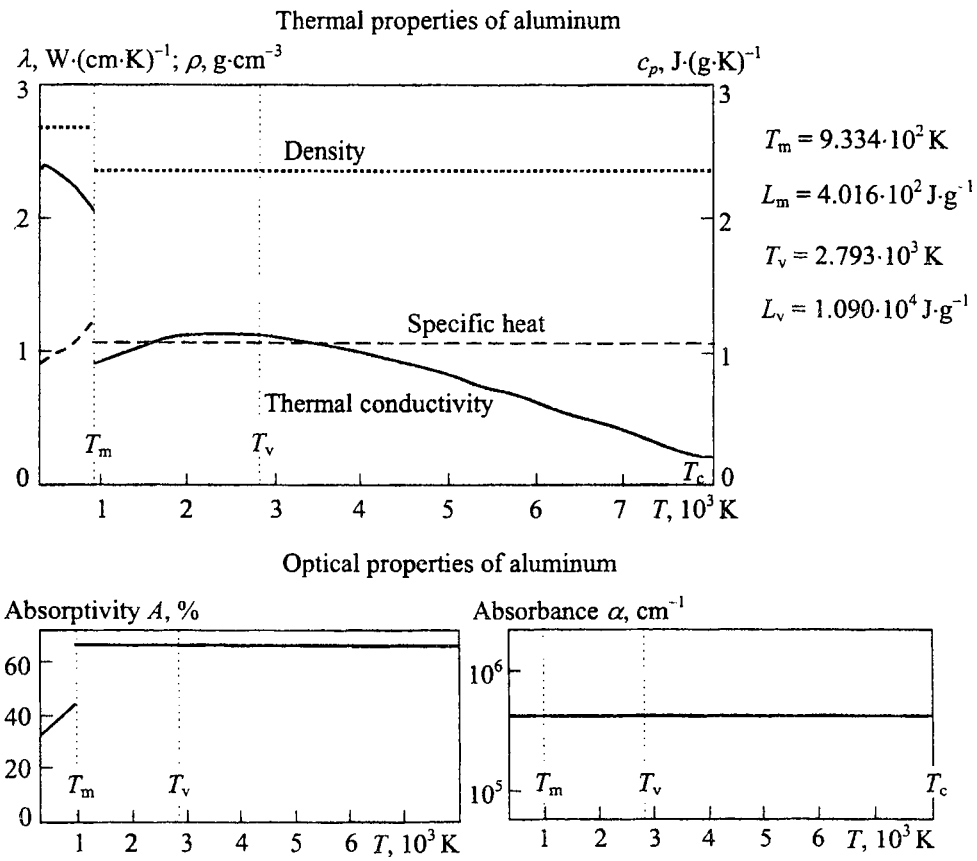

Fig. 2. Thermal and optical characteristics of aluminum.

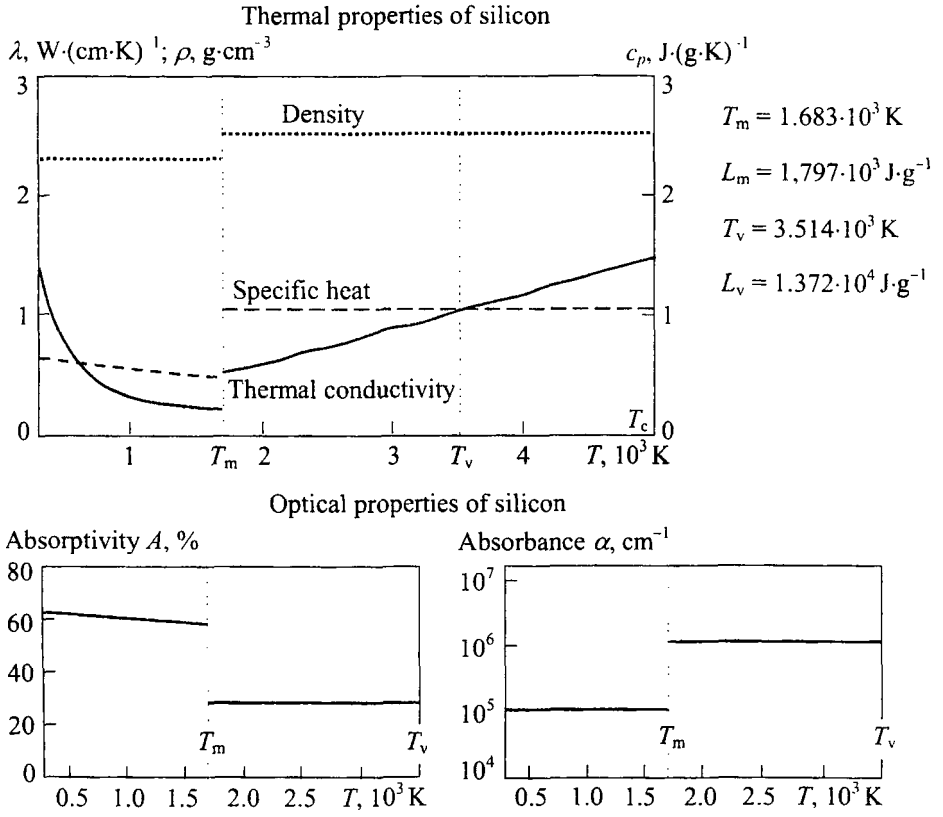

Fig. 3. Thermal and optical characteristics of silicon.

$$r = \delta_l(\delta_l - \delta_s)\exp(-\alpha_l \Delta x_l) + (\delta_s\delta_l - 1)\cos\left(\frac{\alpha_l \Delta x_l n_l}{k_l}\right),$$

$$\gamma = -(\delta_s\delta_l - 1)\sin\left(\frac{\alpha_l \Delta x_l n_l}{k_l}\right),$$

$$a = (\delta_l - \delta_s)(1_l - \delta_l^2),$$

$$\delta_s = \sqrt{R_s}, \quad \delta_l = \sqrt{R_l}.$$

The bulk energy release power in regions k = s, l is given by

$$G_k = k_0 \varepsilon_k'' \frac{|E_k|^2}{|E_0|^2} G_0 \exp\left[-4\left(\frac{t}{\tau_l}\right)^2\right], \qquad (17)$$

where the field strength E_k is normalized to the incident wave field strength E_0 and determined from Maxwell's equations and corresponding boundary conditions on interfaces $x = \Gamma_{lv}$ and $x = \Gamma_{sl}$; $\varepsilon_k'' = 2n_k\kappa_k$ is the imaginary part of the permittivity, and k_0 is the wavenumber of vacuum. The bulk absorbance α_k is expressed in a certain way (see [10]) in terms of the imaginary part κ_k of the complex refractive index $n_k + i\kappa_k$ and the wavelength λ_v,

$$\alpha_k = \frac{4\pi\kappa_k}{\lambda_v}. \qquad (18)$$

Figures 2 and 3 show the temperature dependences of the used thermal and optical characteristics of aluminum and silicon in the condensed state.

2.3. Equations of States

The set (1)–(3) is complemented by the required equations of state formulated as (see [11])

$$H_s = C_{ps}(T_s - T_m),$$

$$p_s = u_{cs}^2 \rho_{0s}\left[\left(\frac{\rho_s}{\rho_{0s}} - 1\right) + \beta_s(T_s - T_0)\right],$$

$$x \in [x_0, \Gamma_{sl}];$$

$$H_l = C_{pl}(T_l - T_m) + L_m, \qquad (19)$$

$$p_l = u_{cl}^2 \rho_{0l}\left[\left(\frac{\rho_l}{\rho_{0l}} - 1\right) + \beta_l(T_l - T_m)\right],$$

$$x \in [\Gamma_{sl}, \Gamma_{sur}].$$

3. SOLUTION METHOD AND ALGORITHM

In the calculation respect, the major difficulty of the solution of Stefan problems is the existence of several (two in this case) mobile boundaries whose position is unknown and should be determined in calculation, taking into account that sizes of solid and liquid subregions during calculation can vary by several orders of magnitude. To solve the Stefan problems, the so-called enthalpy method [12–14] is widely used, in which a moving discontinuity surface in the solution is not explicitly considered, but is replaced by a smoothing procedure. However, the introduction of the latter procedure, which completely excludes the phase boundary from the consideration, and related physical phenomena such as the phase transition kinetics impose natural constraints on the range of applicability of this approach. In problems of pulsed exposure of materials to strong laser fluxes, including analysis of optoacoustic signals, where the absence of the equilibrium of rapid phase transitions can play a crucial role, it becomes necessary to explicitly separate phase boundaries and to consider related processes.

Problem (1)–(20) is numerically solved using the dynamic adaptation method [15, 16] allowing calculation with explicit separation of phase boundaries.

3.1. Dynamic Adaptation Method

The dynamic adaptation method is based on the concept of the transition to an arbitrary non-stationary coordinate system, which is done using the sought-for solution. In this coordinate system, the problem is described by an extended differential set of equations, some of which characterize a physical phenomenon, and others characterize the dynamics of computational grid nodes. The problems associated with mobile boundaries are eliminated using the transition to the arbitrary non-stationary coordinate system with fixed grid nodes and boundaries. The coordinate system is consequentially transformed using the sought-for solution, which allows us to arrange the grid nodes depending on solution features. In non-stationary problems, such features can be the formation and propagation of large-gradient regions, as well as the appearance of discontinuous solutions, i.e., shock waves, contact and phase boundaries. In the former case, grid nodes are concentrated in the region of large gradients using a corresponding transformation function Q depending on the sought-for solution. In the latter case, the appearance of a discontinuous solution within that region is considered as the formation of a new boundary partitioning the initial region into two subregions. Finally, the formation of the new boundary is reduced to the consideration of two boundary-value problems related by a common mobile boundary where corresponding conservation laws are satisfied. The problems associated with mobile boundaries are eliminated by the transition to an arbitrary non-stationary coordinate system with fixed grid nodes and boundaries. The transition from the physical space with variables (x, t) to the calculated space with the arbitrary non-stationary coordinate system (q, τ) is performed by changing the general-form variables $x = f(q, \tau)$ and $t = \tau$ with the inverse nondegenerate transformation $q = \varphi(x, t)$ and $\tau = t$.

In this case, partial derivatives of dependent variables are written as

$$\frac{\partial}{\partial t}=\frac{\partial}{\partial \tau}+\frac{\partial q}{\partial t}\frac{\partial}{\partial q}=\frac{\partial}{\partial \tau}-\frac{\partial x}{\partial \tau}\frac{1}{\psi}\frac{\partial}{\partial q}=\frac{\partial}{\partial \tau}+\frac{Q}{\psi}\frac{\partial}{\partial q},$$
$$\frac{\partial}{\partial x}=\frac{1}{\psi}\frac{\partial}{\partial q},\quad \frac{\partial^2}{\partial x^2}=\frac{1}{\psi}\frac{\partial}{\partial q}\frac{1}{\psi}\frac{\partial}{\partial q}, \tag{20}$$

where $\psi = \partial x/\partial q$ is the metric coefficient and $\partial x/\partial \tau$ is the velocity of the new coordinate system relative to the initial system to be further determined. Relating the coordinate system motion defined by a certain function Q to the sought-for solution features, we derive the inverse transformation equation used then to determine coordinates of computational grid nodes,

$$\frac{\partial x}{\partial \tau}=-Q. \tag{21}$$

The quantities ψ and Q are related by the equation

$$\frac{\partial \psi}{\partial \tau}+\frac{\partial Q}{\partial q}=0 \tag{22}$$

derived by differentiation of Eq. (21) with respect to the space variable q.

Thus, in the transition to the arbitrary non-stationary coordinate system, the initial differential model is transformed to an extended differential set with an additional equation such as (21) or (22), which is the inverse transformation equation. Its type, properties, and form of boundary conditions depend on a specific form of the function Q. To construct grids uniform (quasi-uniform) at each time point in regions with mobile boundaries, the function Q is given as (see [15, 16])

$$\left(Q=-D\frac{\partial \psi}{\partial q}\right)_k,\quad k=\mathrm{s},\mathrm{l},$$

where the diffusivity D is expressed in terms of geometrical and velocity parameters of the problem, $D = L^2(t)(|v_{sl}| + |v_{lv}|)/\Delta x$.

Transforming the general-form variables, we shall write the differential problem (1)–(19) in variables of the arbitrary non-stationary coordinate system (q, τ) in strictly divergent form:

$$\left(\frac{\partial \psi}{\partial \tau} = -\frac{\partial Q}{\partial q}\right)_k, \quad k = \mathrm{s}, \mathrm{l}, \tag{23}$$

$$\left\{\frac{\partial(\psi\rho)}{\partial\tau} + \frac{\partial}{\partial q}\left[\rho(u+Q)\right] = 0\right\}_k,$$

$$\left\{\frac{\partial}{\partial\tau}\left[\psi\rho\left(H + \frac{u^2}{2}\right)\right] + \frac{\partial}{\partial q}\left[\rho(u+Q)\left(H + \frac{u^2}{2}\right)\right]\right.$$

$$\left. = -\frac{\partial}{\partial q}(pu) + \frac{\partial}{\partial q}\left[\frac{\lambda(T)}{\psi}\frac{\partial T}{\partial q}\right]\right\}_k, \tag{24}$$

$$\left\{\frac{\partial}{\partial\tau}(\psi\rho u) + \frac{\partial}{\partial q}\left[\rho u(u+Q)\right] = -\frac{\partial p}{\partial q}\right\}_k,$$

$$\left(\frac{\partial G}{\partial q} + \psi\alpha G\right)_k = 0,$$

$$q \in [0, q_{sl}] \bigcup [q_{sl}, q_s], \quad \tau \in [\tau_0, \tau_{end}], \quad k = \mathrm{s}, \mathrm{l}.$$

3.2. Boundary Conditions

The extended differential model requires additional boundary and initial conditions.

Boundary conditions. When formulating boundary conditions for the inverse transformation equation, propositions common for all Q should be considered, which are as follows.

If there is condition $Q = 0$ among boundary conditions, it means that this boundary is fixed. Any other nonzero relation will characterize the region boundary velocity. Other boundary conditions are written taking into account the appearance of function Q.

• $q = q_0$ is the unperturbed boundary in solid:

$$u = W = 0, \quad Q = 0. \tag{25}$$

• $q = \Gamma_{sl}$ is the solid–liquid interface:

(i) the mass conservation law

$$\rho_s(Q_{sl} + u_s) = \rho_l(Q_{sl} + u_l); \tag{26}$$

(ii) the momentum conservation law

$$P_s + \rho_s(Q_{sl} + u_s)^2 = p_l + \rho_l(Q_{sl} + u_l)^2; \tag{27}$$

(iii) the energy conservation law

$$W_l - W_s = \rho_s v_{sl} L_m^{ne}, \tag{28}$$

where $v_{sl} = -(Q_{sl} + u_s)$.

• $q = \Gamma_{lv}$ is the liquid–vapor interface:

(i) the mass conservation law

$$\rho_l(Q_{lv} + u_l) = \rho_v(Q_{lv} + u_v); \tag{29}$$

(ii) the momentum conservation law

$$P_l + \rho_l(Q_{lv} + u_l)^2 = p_v + \rho_v(Q_{lv} + u_v)^2; \tag{30}$$

(iii) the energy conservation law

$$W_l^T = -\frac{\lambda_l}{\psi_l}\frac{\partial T_l}{\partial q} = \rho_l v_{lv} L_v^{ne}, \qquad v_{lv} = -(Q_{lv} + u_l). \tag{31}$$

Initial conditions. $\tau = \tau_0$: $T_s = T_0$, $u_s = 0$, $\rho_s = \rho_{0.s}$, $\psi = 1$.

3.3. Difference Scheme and Solution Algorithm

The differential model (23)–(31) was numerically solved using the finite-difference method, according to which hydrodynamic equations were approximated by a family of conservative difference schemes obtained by the integro-interpolation method [17]. To construct the family of difference schemes, the grid ω_q^τ with unequal steps $h_{k,i}, \Delta\tau^j$ over spatial q and temporal τ variables is introduced in the calculation space,

$$\omega = \left\{\omega_l \bigcup \omega_s\right\} \times \{\omega_\tau\},$$

where

$$\omega_l = \left\{\begin{array}{l} q_{l,i},\ q_{l,i+1/2};\quad q_{l,i+1} = q_{l,i} + h_{l,i-1},\quad q_{l,i+1/2} = q_{l,i} + 0.5h_{l,i-1}, \\ i = 0,\ldots,N_l - 1,\quad q_{l,0} = 0,\quad q_{N_l} = q_{sl},\quad h_{l,0} = 0,\quad h_{l,N_l+1} = 0 \end{array}\right\},$$

$$\omega_s = \left\{\begin{array}{l} q_{s,i},\ q_{s,i+1/2};\quad q_{s,i+1} = q_{s,i} + h_{s,i+1},\quad q_{s,i+1/2} = q_{s,i} + 0.5h_{s,i+1}, \\ i = 0,\ldots,N_s - 1,\quad q_{s,0} = q_{sl},\quad q_{N_s} = q_s,\quad h_{s,0} = 0,\quad h_{s,N_s+1} = 0 \end{array}\right\}.$$

In the difference approximation of equations, grid functions u, Q, and x relate to nodes with integer indices, and grid functions ρ, P, H, and T relate to points with half-integer indices $(q_{m+1/2}, \tau^j)$.

For differential set (23), (24), the family of difference schemes is written as

$$\left\{\frac{(\psi\rho)^{j+1}_{i+1/2}-(\psi\rho)^{j}_{i+1/2}}{\Delta\tau^{j+1}}+\frac{\left[\rho(u+Q)\right]^{j+1}_{i+1}-\left[\rho(u+Q)\right]^{j+1}_{i}}{h_{i+1}}=0\right\}_k, \tag{32}$$

$$\left\{\frac{(\psi\rho u)^{j+1}_{i+1/2}-(\psi\rho u)^{j}_{i+1/2}}{\Delta\tau^{j+1}}+\frac{\left[\rho u(u+Q)\right]^{j+1}_{i+1}-\left[\rho u(u+Q)\right]^{j+1}_{i}}{h_{i+1}}=-\frac{p^{j+1}_{i+1}-p^{j+1}_{i}}{h_{i+1}}\right\}_k, \tag{33}$$

$$\left\{\frac{\left[\psi\rho\left(\varepsilon+u^2/2\right)\right]^{j+1}_{i+1/2}-\left[\psi\rho\left(\varepsilon+u^2/2\right)\right]^{j}_{i+1/2}}{\Delta\tau^{j+1}}+\frac{\left[\rho(u+Q)\left(\varepsilon+u^2/2\right)\right]^{j+1}_{i+1}-\left[\rho(u+Q)\left(\varepsilon+u^2/2\right)\right]^{j+1}_{i}}{h_{i+1}}\right.$$

$$\left.=-\frac{(pu)^{j+1}_{i+1}-(pu)^{j+1}_{i}}{h_{i+1}}+\frac{1}{h_{i+1}}\left(\frac{\lambda^{j+1}_{i+1}}{\psi^{j+1}_{i+1}}\frac{T^{j+1}_{i+3/2}-T^{j+1}_{i+1/2}}{0.5\left(h_{i+1}+h_i\right)}-\frac{\lambda^{j+1}_{i}}{\psi^{j+1}_{i}}\frac{T^{j+1}_{i+1/2}-T^{j+1}_{i-1/2}}{0.5\left(h_i+h_{i-1}\right)}\right)\right\}_k, \tag{34}$$

$$\left[\frac{\psi^{j+1}_{i+1/2}-\psi^{j}_{i+1/2}}{\Delta\tau^{j+1}}=-\frac{Q^{j+1}_{i+1}-Q^{j+1}_{i}}{h_{i+1}}\right]_k, \quad \left[Q^{j+1}_i=-D^j_i\frac{\psi^{j+1}_{i+1/2}-\psi^{j+1}_{i-1/2}}{\left(h_i+h_{i+1}\right)/2}\right], \tag{35}$$

$$\left[\frac{x^{j+1}_{i+1}-x^{j+1}_{i}}{h_{i+1}}=\psi^{j+1}_{i+1/2}\right]_k, \tag{36}$$

where $i=0,\ldots,N_l-1$ at $k=$ l, $i=0,\ldots,N_s-1$ at $k=$ s.

The values at half-integer nodes for grid functions related to integer points are calculated as a halfsum of values at the nearest nodes. When determining the values at nodes with integer indices for functions related to half-integer points, the linear interpolation

$$y_m=\frac{y_{m-1/2}\psi_{m+1/2}+y_{m+1/2}\psi_{m-1/2}}{\psi_{m+1/2}+\psi_{m-1/2}}$$

is used.

Difference schemes (32)–(36) were numerically implemented using a special algorithm consisting of several embedded iteration cycles [11, 16]. The computing process for a single time step is schematically shown in Fig. 4. According to this scheme, the algorithm consists of three inner and one outer iteration procedures. When passing from the jth to $j+1$th time layer, computation is performed in the following sequence. First, nonlinear equations (26)–(31) are solved at boundaries Γ_{sl} and Γ_{lv} by the Newton iteration method, and inner iteration cycles are executed in each phase region using known values of Q_{sl} and Q_{lv}.

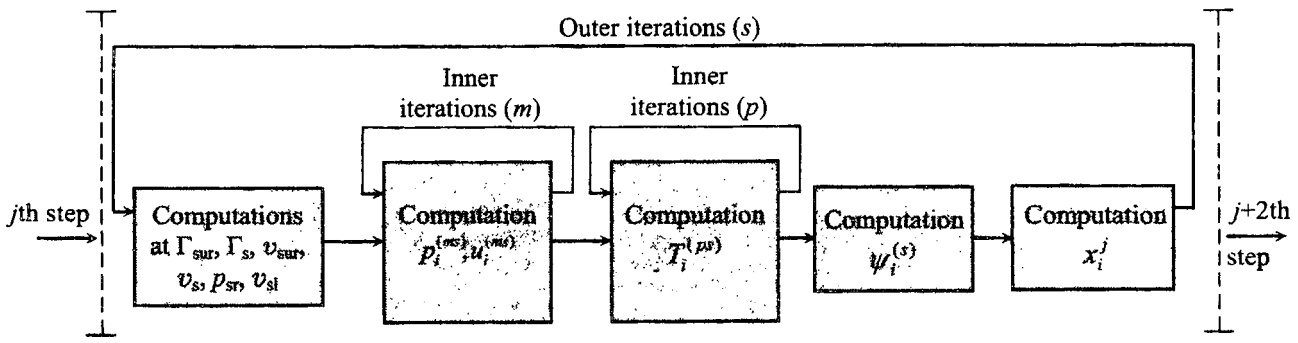

Fig. 4. Block diagram of the computing process.

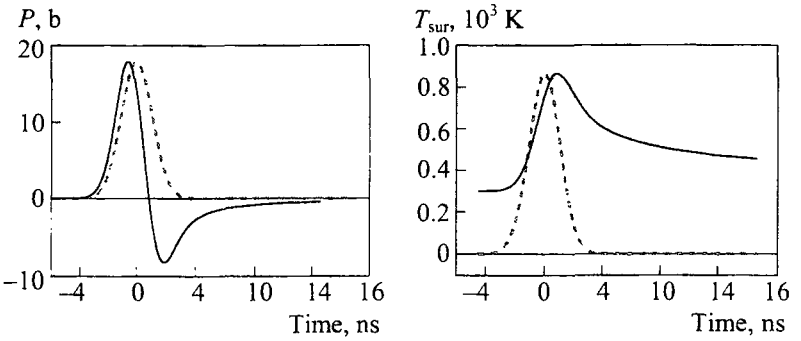

Fig. 5. Time dependences of the pressure $P(t)$ and temperature $T_{sur}(t)$ (solid curves), as well as the absorbed intensity in relative units (dashed curve) in aluminum at $G_0 = 30\,\mathrm{MW\cdot cm^{-2}}$ and $\tau_1 = 3\cdot10^{-9}$ s.

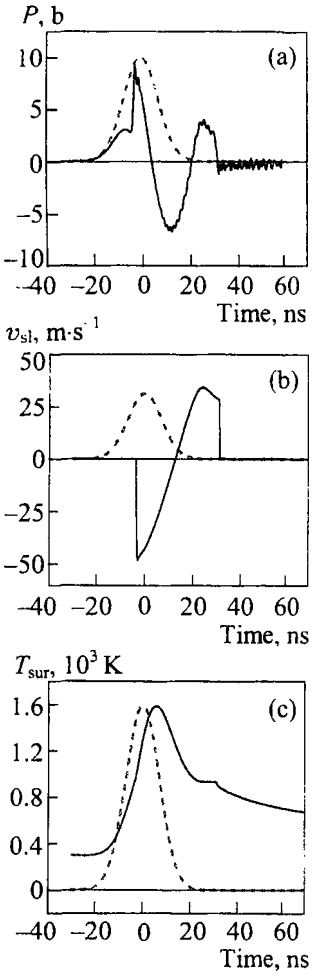

Fig. 6

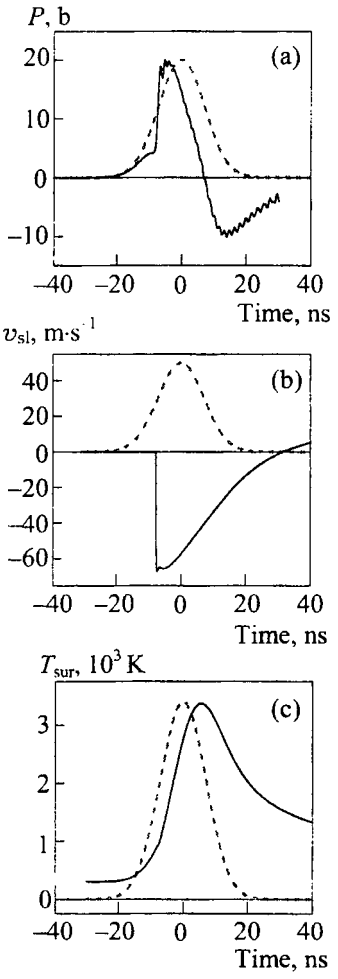

Fig. 7

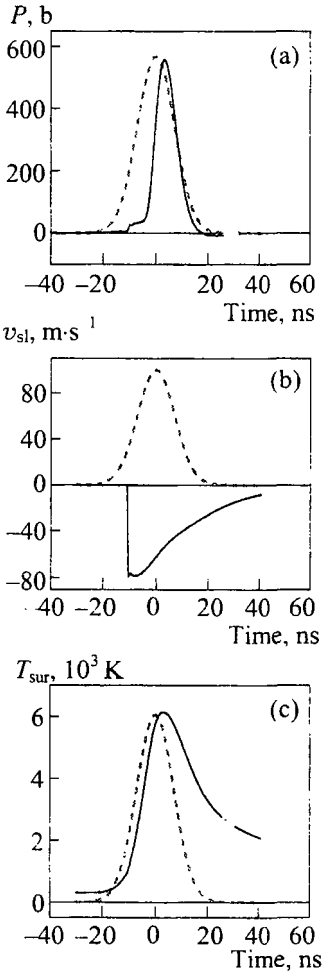

Fig. 8

Fig. 6. Time dependences of the pressure $P(t)$, melting velocity $v_{sl}(t)$, temperature $T_{sur}(t)$ (solid curves), and absorbed intensity in relative units (dashed curves) in aluminum at $G_0 = 25\,\mathrm{MW\cdot cm^{-2}}$, $A = 100\,\%$, and $\tau_1 = 2\cdot10^{-8}$ s.

Fig. 7. The same as in Fig. 6 but for $G_0 = 50\,\mathrm{MW\cdot cm^{-2}}$.

Fig. 8. The same as in Fig. 6 but for $G_0 = 100\,\mathrm{MW\cdot cm^{-2}}$.

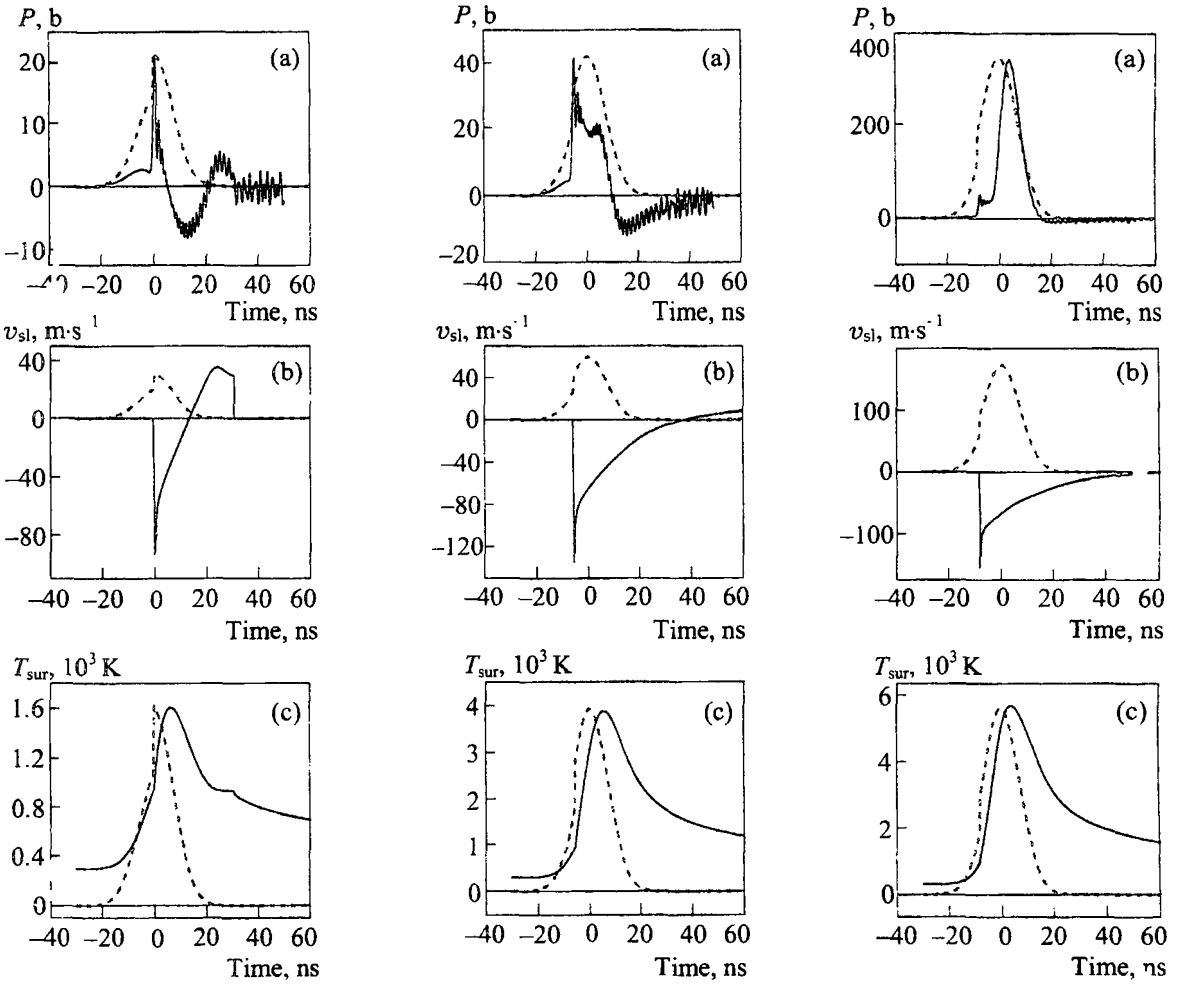

Fig. 9 Fig. 10 Fig. 11

Fig. 9. Time dependences of the pressure $P(t)$, melting velocity $v_{sl}(t)$, temperature $T_{sur}(t)$ (solid curves), and absorbed intensity in relative units (dashed curves) in aluminum at $G_0 = 50$ MW·cm^{-2}, $A = A(T_{sur})$, and $\tau_l = 2 \cdot 10^{-8}$ s.

Fig. 10. The same as in Fig. 9 but for $G_0 = 100$ MW·cm^{-2}.

Fig. 11. The same as in Fig. 9 but for $G_0 = 150$ MW·cm^{-2}.

In the iteration cycle with index m, residuals of hydrodynamic functions ρ_i^m and u_i^m are calculated; from the second iteration cycle with index p, residuals of the function T_i^p are determined at each iteration cycle using double-sweep method.

As convergence in inner cycles is reached, the outer iteration cycle begins to execute, in which the values of function ψ_i^j are determined using Eq. (32), and the values of velocities at phase boundaries Γ_{sl} and Γ_{lv} are redetermined by the known values of functions ρ_i^m, u_i^m, and T_i^p. The values of functions were considered as calculated at the time step τ^{j+1}, if the outer iteration cycle converged. When passing to the next time layer, the coordinates x_i^j of grid nodes in the physical space are redetermined using relation (36).

Computing process discretization into separate iteration significantly accelerates convergence of iteration cycles and makes it possible to decrease several times the computing time in comparison with calculation using a single iteration scheme. The main advantage of the used algorithm is the fact that the transition to the arbitrary non-stationary coordinate system eliminates difficulties associated with mobile boundaries and allows one to calculate using through calculation formulas.

4. ANALYSIS OF SIMULATION RESULTS

For strongly absorbing media without phase transitions in the heating region, the photoacoustic signal (Fig. 5) is approximately proportional to the time derivative of the irradiated surface temperature and has a characteristic bipolar shape. Its positive phase amplitude approximately twice exceeds the negative phase amplitude, if the laser pulse is Gaussian [1].

Melting significantly changes the photoacoustic signal shape. Figures 6–8 show the behavior of the pressure pulse $P(t)$, melting front velocity $v_{sl}(t)$, and surface temperature $T_{sur}(t)$ of an aluminum target irradiated with a laser pulse with $\tau_l = 20$ ns and peak intensities of 25 (Fig. 6), 50 (Fig. 7), and 100 MW·cm^{-2} (Fig. 8) at constant absorptivity $A = 1$. The pressure pulse position on the time axis corresponds to the zero sound delay, i.e., is related to the irradiated surface position.

The sharp increase in the pressure in Figs. 6(a) and 7(a) corresponds to the melting onset time and is caused mainly by a change in the density that decreases for aluminum upon melting. Such a conclusion is based on satisfactory agreement of the value of this jump with the maximum velocity of the melting front according to the simple estimate $P = \Delta\rho v_{sl}^2$ [1].

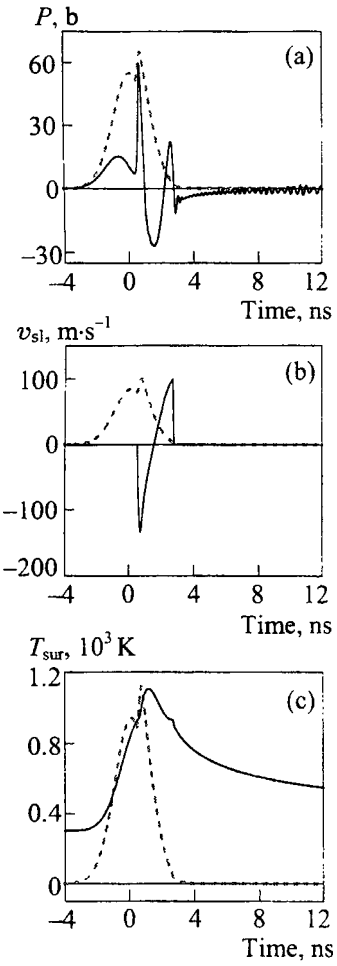

Fig. 12

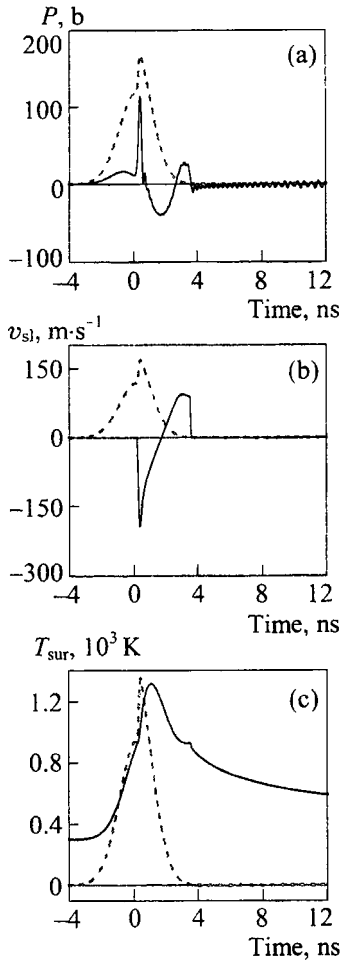

Fig. 13

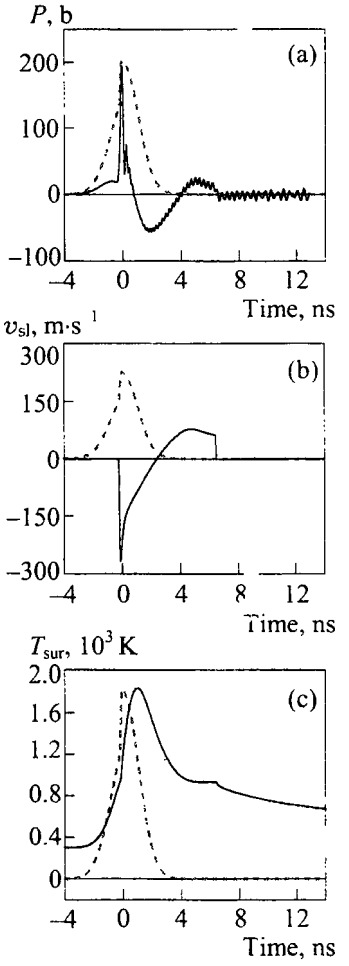

Fig. 14

Fig. 12. Time dependences of the pressure $P(t)$, melting velocity $v_{sl}(t)$, temperature $T_{sur}(t)$ (solid curves), and absorbed intensity in relative units (dashed curves) in aluminum at $G_0 = 110$ MW·cm^{-2}, $A = A(T_{sur})$, and $\tau_l = 3 \cdot 10^{-9}$ s.

Fig. 13. The same as in Fig. 12 but for $G_0 = 120$ MW·cm^{-2}.

Fig. 14. The same as in Fig. 12 but for $G_0 = 150$ MW·cm^{-2}.

The behavior of the photoacoustic signal is also appreciably affected by changes in the enthalpy and other thermal parameters at the solid–liquid phase transition.

The increase in the peak value of the absorbed intensity from 50 to 100 MW·cm^{-2} is accompanied by almost 30-fold pressure increase (Fig. 8(a)), whose value is now caused by the evaporation. A further increase in the intensity can lead to plasma formation in the evaporated material flow, which is not considered in this study.

The assumption on the constant absorptivity $A = 1$ can be considered as satisfactory for rather short-wavelength radiation. In infrared and visible regions, the difference of A from unity already cannot be ignored, since its variation during the laser pulse has a significant effect on the shape and value of the photoacoustic signal.

The behavior of the photoacoustic signal $P(t)$, taking into account the absorptivity variation, is shown in Figs. 9–11, as well as $v_{sl}(t)$ and $T_{sur}(t)$, for incident radiation intensities of 50, 100, and 150 MW·cm^{-2}. A comparison of Figs. 9(a) and 11(a) shows that an increase in A upon melting results in an increase in the pressure jump, caused by melting, and a decrease in its duration. The latter becomes shorter than the laser pulse duration approximately by an order of magnitude. The time dependence of the melting front velocity shows similar changes. Such changes in the behavior of the photoacoustic signal $P(t)$ and melting front

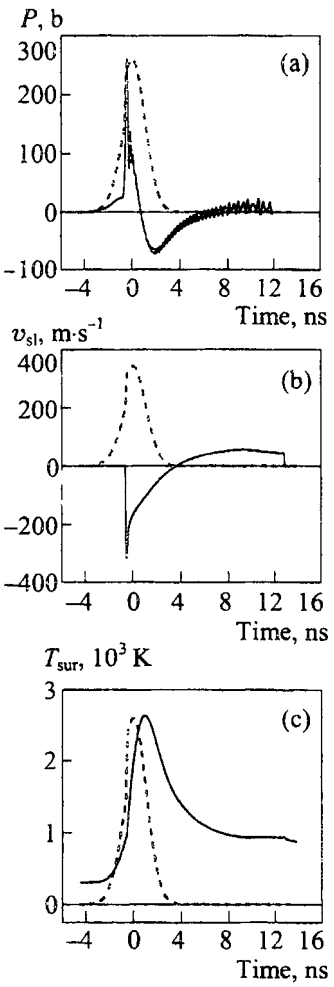

Fig. 15

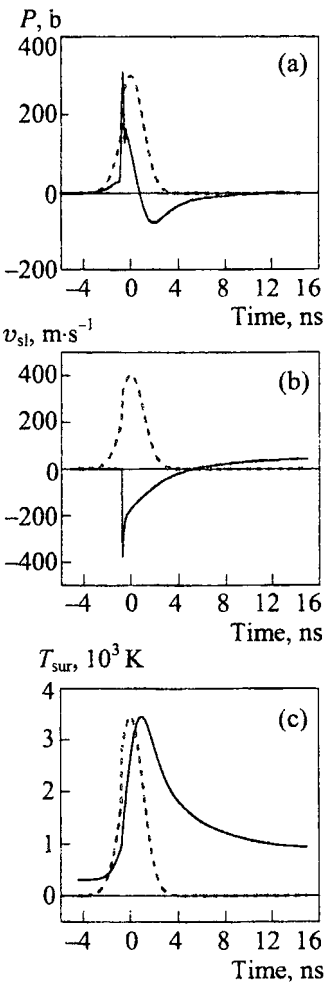

Fig. 16

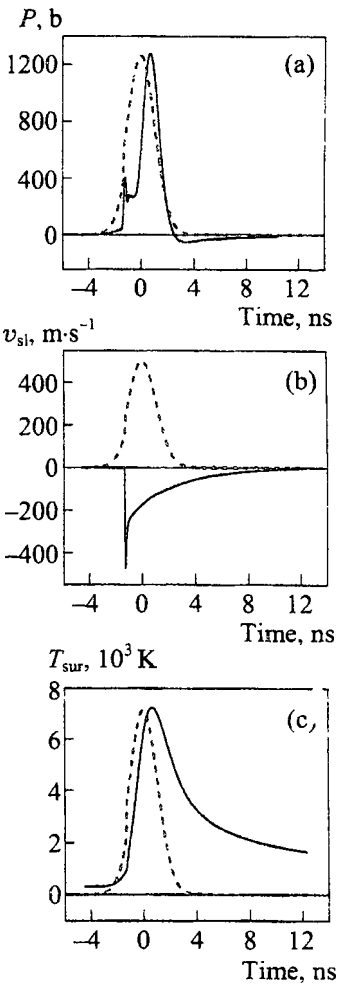

Fig. 17

Fig. 15. Time dependences of the pressure $P(t)$, melting velocity $v_{sl}(t)$, temperature $T_{sur}(t)$ (solid curves), and absorbed intensity in relative units (dashed curves) in aluminum at $G_0 = 200$ MW·cm^{-2}, $A = A(T_{sur})$, and $\tau_l = 3 \cdot 10^{-9}$ s.

Fig. 16. The same as in Fig. 15 but for $G_0 = 250$ MW·cm^{-2}.

Fig. 17. The same as in Fig. 15 but for $G_0 = 500$ MW·cm^{-2}.

velocity $v_{sl}(t)$ are in fact caused by efficient steepening of the leading edge of the absorbed laser pulse, which occurs when A rapidly increases.

It is clear that a relative increase and shortening in the photoacoustic signal $P(t)$ with simultaneous shortening of the duration of melting and solidification will also occur when using shorter laser pulses. At $\tau_l = 3$ ns, the behavior of the pressure, melting–solidification front velocity, and temperature of the irradiated aluminum surface is shown in Figs. 12–17 in the intensity range 110–500 MW·cm^{-2}.

As the intensity increases, the maximum front velocity and melting phase duration also increase. However, the maximum velocity of the solidification front decreases in this case, and the solidification phase duration increases more rapidly than the laser pulse intensity. The increase in the positive phase of the photoacoustic signal, associated with shortening of the laser pulse duration, results in that this signal remains noticeable at significantly larger evaporation pressures (Figs. 12(a)–14(a)). It should be noted that experimental observation of a subnanosecond structure of pressure pulses can be a rather complex problem. We also recall that a sharp enough pressure decrease in an irradiated material is a factor stimulating the beginning of decomposition of the overheated metastable phase under certain conditions [1].

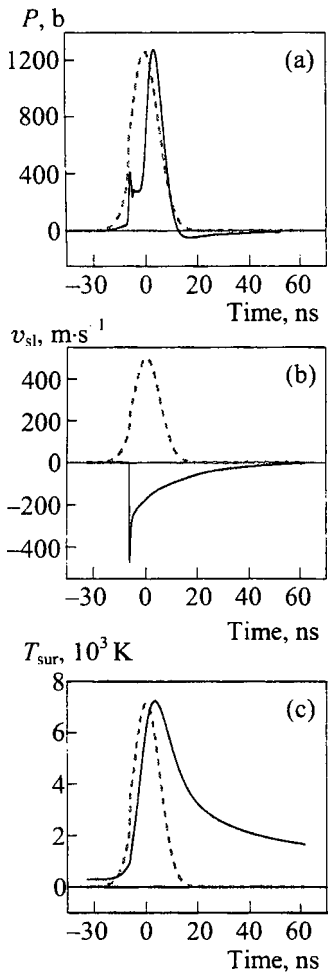

Fig. 18

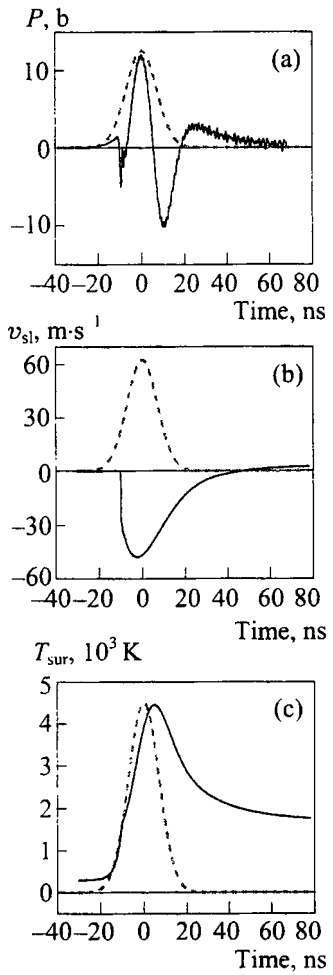

Fig. 19

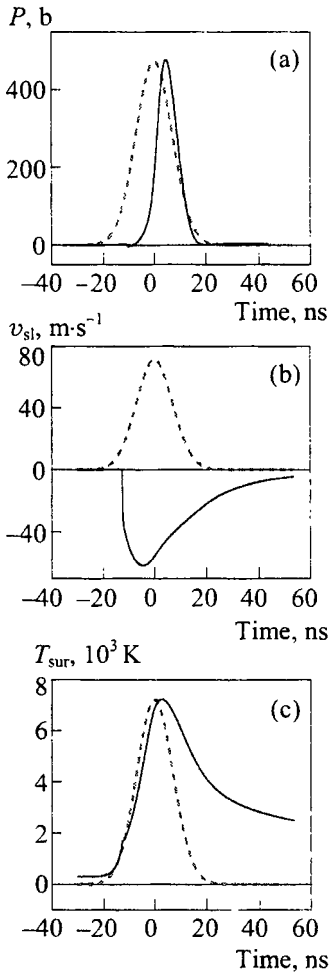

Fig. 20

Fig. 18. Time dependences of the pressure $P(t)$, melting velocity $v_{sl}(t)$, temperature $T_{sur}(t)$ (solid curves), and absorbed intensity in relative units (dashed curves) in silicon at $G_0 = 25$ MW·cm^{-2}, $A = 100\%$, and $\tau_l = 2 \cdot 10^{-8}$ s.

Fig. 19. The same as in Fig. 18 but for $G_0 = 50$ MW·cm^{-2}.

Fig. 20. The same as in Fig. 18 but for $G_0 = 100$ MW·cm^{-2}.

As noted above, the pressure jump (additional in comparison with the single-phase case) in the photoacoustic signal in aluminum is caused by a decrease in the aluminum density and reflectivity upon melting. An opposite-sign contribution to this effect is made by the enthalpy jump at the phase transition, i.e., energy absorption at the melting front. Similar changes will be caused by an increase in the reflectivity and density of an irradiated material upon melting which occurs, for example, for silicon. In this case, a rather narrow dip should be observed instead of a positive pressure jump against the background of the photoacoustic signal.

The behavior of $P_{ph}(t)$, $v_{sl}(t)$, and $T_{sur}(t)$ for silicon exposed to a laser pulse with $\tau_l = 20$ ns in the intensity range $G_0 = 25$–$100\,\mathrm{MW\cdot cm^{-2}}$ and on the assumption of constant absorptivity $A = 1$ is shown in Figs. 18–20. The dip in the photoacoustic signal is most noticeable at small intensity excesses above the melting threshold (Figs. 18(a) and 19(a)); in contrast to aluminum, the effect of melting is already almost indistinguishable against the background of the evaporation pressure $G_0 = 100\,\mathrm{MW\cdot cm^{-2}}$ (Fig. 20(a)) (cf. Figs. 8(a) and 10(a)).

5. CONCLUSION

The results of numerical simulation of the photoacoustic signal in the presence of the first-order phase transitions in an irradiated target show, in particular, that the melting front velocity can be determined by the additional pressure pulse caused by melting. The width of this additional pulse is very small in comparison with the laser pulse duration. Therefore, experimental detection of such features in the photoacoustic signal requires a sufficiently uniform (constant) intensity distribution over the irradiation spot.

The considered results do not pretend to exhaustive description of the melting process, since they were obtained ignoring, for example, features in the melting front dynamics, associated with possible initial overheating of the solid phase and other dynamic and nonequilibrium effects at the transition front (see, for example, [18–20] and references therein about these effects). In principle, these effects can be considered within the described approach. However, it is more advantageous to perform such a detailed analysis in direct connection with corresponding experimental data which are still not obtained. We expect that the results of this study will promote performance of such experiments.

It should be noted in conclusion some effects in laser evaporation process, which are due to plasma formation in vapor plume above an irradiated surface. Laser light absorption in plasma leads to an increase in temperature T and pressure p in evaporated matter. When the pressure p exceeds the saturation pressure $P(T)$ corresponding to the surface temperature T, condensation can occur at the irradiated surface instead of evaporation [1, 6, 21]. In contrast to the evaporation process which depends on single external gasdynamic parameter [7, 8, 22, 23], the condensation is determined by two such parameters [24]. If the difference P–p becomes positive, the gasdynamic evaporation process begins again with the formation of contact jump between vapor and plasma layers. In this region, the heat and mass diffusion processes are important because of large temperature and concentration gradients. This situation is analogous to the case when gasdynamic evaporation process develops in the presence of an ambient gas above the irradiated surface. As far as we know, boundary conditions for such cases have not been analyzed yet.

ACKNOWLEDGMENTS

This work was partially supported by RFBR Projects 07-07-00045 and 06-08-01440.

REFERENCES

1. *Effect of Laser Radiation on Absorbing Condensed Media*, Vol. 13, Ed. by V. B. Fedorov (Nauka, Moscow, 1988) [in Russian].
2. V. E. Gusev and A. A. Karabutov, *Laser Optoacoustics* (Nauka, Moscow, 1991) [in Russian].
3. G. Paltauf and P. E. Dyer, "Photomechanical Processes and Effects in Ablation," Chem. Rev. **103**, 487 (2003).
4. H. Carslaw and J. Jaeger, *Conduction of Heat in Solids* (Clarendon, Oxford, 1959).
5. J. I. Masters, "Problem of Intense Surface Heating of a Slab Accompanied by Change of Phase," J. Appl. Phys. **27**, 477 (1956).
6. V. I. Mazhukin and A. A. Samarskii, "Mathematical Modeling in the Technology of Laser Treatments of Materials," Surveys on Mathematics for Industry **4**(2), 85 (1994).
7. D. Crout, "An Application of Kinetic Theory to the Problems of Evaporation and Sublimation of Monatomic Gases," J. Math. Phys. **15**, 1 (1936).
8. V. I. Mazhukin, P. A. Prudkovskii, and A. A. Samokhin, "About Gas-Dynamical Boundary Conditions on Evaporation Front," Mathematical Modeling **5**(3), 3 (1993).
9. L. D. Landau and E. M. Lifshitz, *Electrodynamics of Continuous Media* (Pergamon, Oxford, 1989).

10. A. F. Aleksandrov, L. S. Bogdankevich, and A. A. Rukhadze, *Fundamentals of Plasma Electrodynamics* (Vysshaya Shkola, Moscow, 1978) [in Russian].
11. V. V. Nosov and V. I. Mazhukin, "Influence of Melting and Crystallization Processes on the Optoacoustic Signal Shape during Laser Exposure of Strongly Absorbing Condensed Media," Matematicheskoe Modelirovanie. **6**(1), 3 (1994) [Mathematical Modeling].
12. A. A. Samarsky and B. D. Moiseenko, "Economic Scheme of Through Calculation for the Stefan Multivariate Problem," Zh. Vychisl. Mat. Mat. Fiz. **5**(5), 816 (1965) [Comput. Math. Math. Phys.].
13. B. M. Budak, E. N. Solovieva, and A. B. Uspensky, "Difference Method with Smoothing of Coefficients for Solving the Stefan Problem," Zh. Vychisl. Mat. Mat. Fiz. **5**(5), 828 (1965) [Comput. Math. Math. Phys.].
14. G. H. Meyer, "The Numerical Solution of Stefan Problems with Front-Tracking and Smoothing Methods," Appl. Math. Comput. **4**, 283 (1978).
15. P. V. Breslavsky and V. I. Mazhukin, "Mathematical Modeling of Pulsed Melting and Evaporation of Metal with Explicit Separation of Phase Boundaries," Inzh. Fiz. Zh. **57**(1), 107 (1989) [J. Eng. Phys.].
16. P. V. Breslavsky and V. I. Mazhukin, "Algorithm of Numerical Solution of the Hydrodynamic Version of the Stefan Problem using Adapting Grids," Matematicheskoe Modelirovanie. **3**(10), 104 (1991) [Mathematical Modeling].
17. A. A. Samarsky, *Theory of Difference Schemes* (Nauka, Moscow, 1989) [in Russian].
18. P. V. Breslavsky, V. I. Mazhukin, and A. A. Samokhin, "About the Hydrodynamic Version of the Stefan Problem for Material in the Metastable State," Dokl. Acad. Nauk SSSR **320**(3), 1078 (199[illegible] [Sov. Phys.-Dokl.].
19. Ch. Charach and I. Rubinstein, "Pressure-Temperature Effects in Planar Problems with Density Change," J. Appl. Phys. **73**(3), 1128 (1992).
20. K. Vetsigian and N. Goldenfeld, "Computationally Efficient Phase-Field Model with Interface Kinetics," Phys. Rev. E. **68**(4), 060601 (2003).
21. V. I. Mazhukin, V. V. Nossov, and I. Smurov, "Modeling of Plasma-Controlled Evaporation and Surface Condensation of Al Induced by 1.06 and 0.248 μm Laser Radiations," J. Appl. Phys. **101**, 024922 (2007).
22. A. V. Gusarov and I. Smurov, " Gas-Dynamic Boundary Conditions of Evaporation and Condensation: Numerical Analysis of the Knudsen Layer," Phys. Fluids. **14**, 4242 (2002).
23. I. N. Kartashov, A. A. Samokhin, and I. Yu. Smurov, "Boundary Conditions and Evaporation Instabilities," J. Phys. D: Appl. Phys. **38**, 3703 (2006)
24. Y. Sone, S. Takata, and F. Golse, "Note on the Boundary Conditions for Fluid Dynamic Equations on the Interface of a Gas and Its Condensed Phase," Phys. Fluids. **13**, 324 (2001).